Simon, H., Buske, S., Krau, F., Giese, R., Hedin, P., Juhlin, C. (2017): The derivation of an anisotropic velocity model from a combined surface and borehole seismic survey in crystalline environment at the COSC-1 borehole, central Sweden. - *Geophysical Journal International*, *210*, 3, pp. 1332—1346.

DOI: http://doi.org/10.1093/gji/ggx223

Geophysical Journal International

Geophys. J. Int. (2017) **210,** 1332–1346
Advance Access publication 2017 May 20
GJI Seismology

doi: 10.1093/gji/ggx223

The derivation of an anisotropic velocity model from a combined surface and borehole seismic survey in crystalline environment at the COSC-1 borehole, central Sweden

H. Simon,[1] S. Buske,[1] F. Krauß,[2] R. Giese,[2] P. Hedin[3] and C. Juhlin[3]

[1]*Institute of Geophysics and Geoinformatics, TU Bergakademie Freiberg, D-*09596 *Freiberg, Germany. E-mail: helge.simon@geophysik.tu-freiberg.de*
[2]*Centre for Scientific Drilling, GFZ German Research Centre for Geosciences - Helmholtz Centre Potsdam, D-*14473 *Potsdam, Germany*
[3]*Department of Earth Sciences, Uppsala University,* 751 05 *Uppsala, Sweden*

Accepted 2017 May 19. Received 2017 May 18; in original form 2016 October 13

SUMMARY

The Scandinavian Caledonides provide a well-preserved example of a Palaeozoic continent–continent collision, where surface geology in combination with geophysical data provides information about the geometry of parts of the Caledonian structure. The project COSC (Collisional Orogeny in the Scandinavian Caledonides) investigates the structure and physical conditions of the orogen units and the underlying basement with two approximately 2.5 km deep cored boreholes in western Jämtland, central Sweden. In 2014, the COSC-1 borehole was successfully drilled through a thick section of the Seve Nappe Complex. This tectonostratigraphic unit, mainly consisting of gneisses, belongs to the so-called Middle Allochthons and has been ductilely deformed and transported during the collisional orogeny. After the drilling, a major seismic survey was conducted in and around the COSC-1 borehole with the aim to recover findings on the structure around the borehole from core analysis and downhole logging. The survey comprised both seismic reflection and transmission experiments, and included zero-offset and multiazimuthal walkaway Vertical Seismic Profile (VSP) measurements, three long offset surface lines centred on the borehole, and a limited 3-D seismic survey. In this study, the data from the multiazimuthal walkaway VSP and the surface lines were used to derive detailed velocity models around the COSC-1 borehole by inverting the first-arrival traveltimes. The comparison of velocities from these tomography results with a velocity function calculated directly from the zero-offset VSP revealed clear differences in velocities for horizontally and vertically travelling waves. Therefore, an anisotropic VTI (transversely isotropic with vertical axis of symmetry) model was found that explains first-arrival traveltimes from both the surface and borehole seismic data. The model is described by a vertical *P*-wave velocity function derived from zero-offset VSP and the Thomsen parameters $\epsilon = 0.03$ and $\delta = 0.3$, estimated by laboratory studies and the analysis of the surface seismic and walkaway VSP data. This resulting anisotropic model provides the basis for further detailed geological and geophysical investigations in the direct vicinity of the borehole.

Key words: Composition and structure of the continental crust; Downhole methods; Controlled source seismology; Seismic anisotropy; Seismic tomography; Crustal structure.

1 INTRODUCTION

The Scandinavian Caledonides, a part of the North Atlantic Caledonides, provide a well preserved deeply eroded example of a Palaeozoic continent-continent collision. The International Continental scientific Drilling Program (ICDP) project COSC (Collisional Orogeny in the Scandinavian Caledonides), led by the Swedish Scientific Drilling Program (SSDP), focuses on the Caledonian Orogen (Gee *et al.* 2010; Lorenz *et al.* 2011) in order to better understand orogenic processes from the past and in recently active mountain belts, like the Himalayas (see e.g. Andersen 1998; Streule *et al.* 2010). The structure and physical conditions (e.g. resistivity, elastic wave velocity, density, temperature, permeability, differential stress) of the orogen units, in particular of the Seve Nappe Complex (SNC, 'hot' allochthon), the Lower Allochthon and the underlying basement, will be investigated with two approximately 2.5 km deep fully cored scientific boreholes in the Swedish province Jämtland (central Sweden).

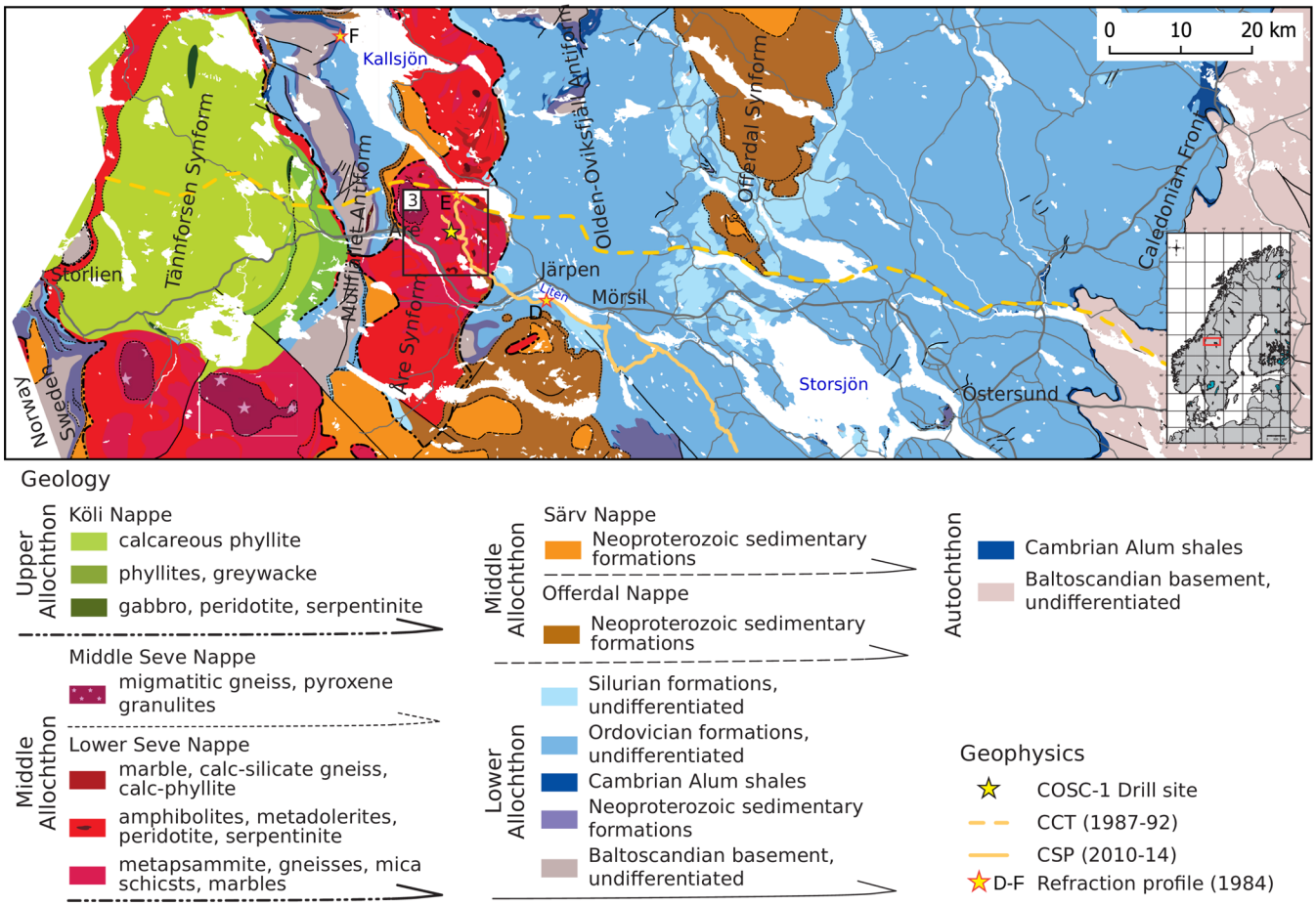

Figure 1. Regional tectonostratigraphic map (based on the bedrock geological map of Sweden, © Geological Survey of Sweden (I2014/00601) and Strömberg *et al.* (1984)) showing the relations between the different Caledonian nappes and the underlying autochthonous basement. The previous seismic profiles of the area are marked. The black rectangle indicates the location of the acquisition map in Fig. 3.

1.1 Geological setting

The formation of the Caledonian orogen started in the late Ordovician as a consequence of the closure of the Iapetus Ocean, which caused the collision between the palaeocontinents Laurentia and Baltica during Silurian times, about 440 Ma ago (Gee *et al.* 2008; Ladenberger *et al.* 2014). The collision caused underthrusting of Baltica beneath Laurentia and resulted in the thickening and shortening of the crust. Several hundreds of kilometres of east-directed (onto the Baltoscandian platform) and west-directed (onto the Laurentian platform of Greenland) thrust emplacements of allochthons have been identified (Gee 1978). After three hundred million years of erosion and the uplift and extension during the Cenozoic opening of the North Atlantic Ocean, the orogen today exposes mid-crustal rocks in Norway and western Sweden. Additionally, the Scandinavian Caledonides have not experienced more recent orogenic overprint and, thus it presents a unique possibility to study thrust and extensional tectonics (e.g. Gee 1975, 1978; Andersen 1998). Surface geology, in combination with geophysical data provide information about the large scale geometry of the present-day Caledonian structure. This structure consists of the allochthons and the underlying autochthon units, and the shallow west-dipping décollement surface that separates the two units and consists of a thin skin of Cambrian black shales.

But due to very few accessible exposed outcrops, only samples from the drillcore will provide the opportunity to study the rock material directly involved in the mountain building process of the Scandinavian Caledonides. Also, some questions concerning the active formation of the mountains, like the emplacement of hot allochthons (Ladenberger *et al.* 2014; Grimmer *et al.* 2015) and the generation of ultrahigh pressure rocks (Majka *et al.* 2014), can only be answered by drilling *in situ* rock material and investigating physical parameters through geophysical logging.

The purpose of the first borehole COSC-1 was therefore, to sample an as-thick-as-possible section of the lower units of the high grade metamorphic (partly ultrahigh pressure metamorphism (Majka *et al.* 2014; Klonowska *et al.* 2015)) SNC (see Fig. 1), which belongs to the so-called Middle Allochthons (Gee & Sturt 1985), and to go further down into the underlying thrust zone. The rocks of the SNC have their origin at the outer margins of the Baltica palaeocontinent and partly at the continent-ocean-transition zones (Andréasson 1994). In the initial stages of the Caledonian orogeny they were partially subducted to great depths, then deformed ductilely and emplaced hot onto the underlying allochthons (Klonowska *et al.* 2014; Ladenberger *et al.* 2014). Fig. 2 shows a simplified sketch of the relationship between the borehole and the main structural units. The second borehole COSC-2 will be drilled later through the underlying Lower Allochthons (Ordovician turbidities), penetrating the major basal detachment zone (closely associated with a thin layer of Cambrian black alum shales) and reaching into the highly reflective Precambrian crystalline

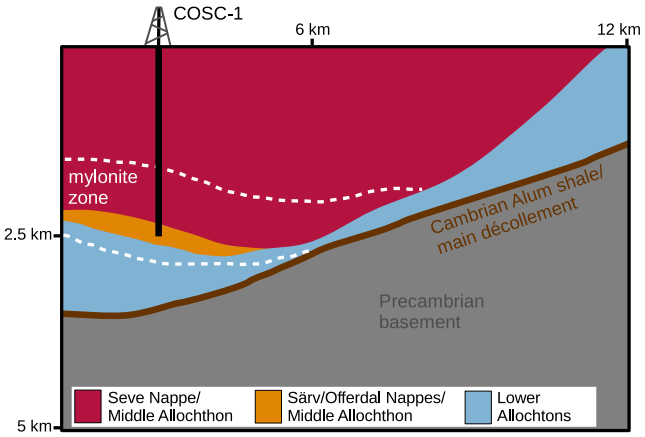

Figure 2. Simplified geological sketch section showing the main structural units in relation to the borehole COSC-1 along the northwestern part of the CSP (after Juhlin *et al.* 2016).

basement. Both drillcores together will form a unique 5 km long section through the Caledonian orogen.

1.2 Previous geophysical investigations

During the last *c.* 40 years a wide range of geophysical and geological investigations have been conducted in the Scandinavian Caledonides (e.g. Gee 1975; Gee & Sturt 1985; Roberts 2003; Gee *et al.* 2008; Corfu *et al.* 2014). In particular, the central part of the mountain belt was extensively investigated (Dyrelius *et al.* 1980; Dyrelius 1985) along the so-called Central Caledonian Transect (CCT), a 300 km long, deep seismic reflection survey crossing the belt from the Caledonian thrust front in Jämtland (Sweden) to the Atlantic coast of Norway. The profile reveals a very reflective upper crust and large scale structures, which are related both to the emplacement of the nappes and the Caledonian deformation, and also the deeper parts of the crust down to the Moho (Hurich *et al.* 1989; Palm *et al.* 1991; Juhojuntti *et al.* 2001). Further studies in the same area based on different geophysical methods, like potential field investigations (Dyrelius *et al.* 1980; Dyrelius 1986; Elming 1988; Ebbing *et al.* 2012; Hedin *et al.* 2014), magnetotellurics (Korja *et al.* 2008), and additional (to the CCT) active (Palm & Lund 1980; Palm 1984; Schmidt 2000; Lund *et al.* 2001) and passive (England & Ebbing 2012) seismic investigations, have contributed to improve the understanding of the Caledonian orogen.

For our study, the seismic refraction investigations by Palm (1984) are of particular interest. They aimed to investigate the structure of the Precambrian basement in the Caledonian Front, but one of the profiles (see Fig. 1) also covered the Caledonian SNC. The recorded velocities with values between 6.2 and 6.35 km s^{-1} are generally high, and even higher than the underlying crystalline basement velocities (5.8–6.0 km s^{-1}).

More recent high resolution reflection seismic profiles (CSP, COSC Seismic Profile, see Fig. 1; Hedin *et al.* 2012; Juhlin *et al.* 2016) and a complementary magnetotelluric survey (Yan *et al.* 2016) in Jämtland provided detailed images of the upper 8–10 kilometres of the subsurface. These images, together with the CCT and data from older shallow drillholes further to the east, allow for a detailed geological interpretation of the major tectonic structures in the area, and led to the siting of the two COSC boreholes. In particular the SNC was resolved as a highly reflective area, but very little information about the internal structure of the nappe complex could be extracted from surface reflection seismic data

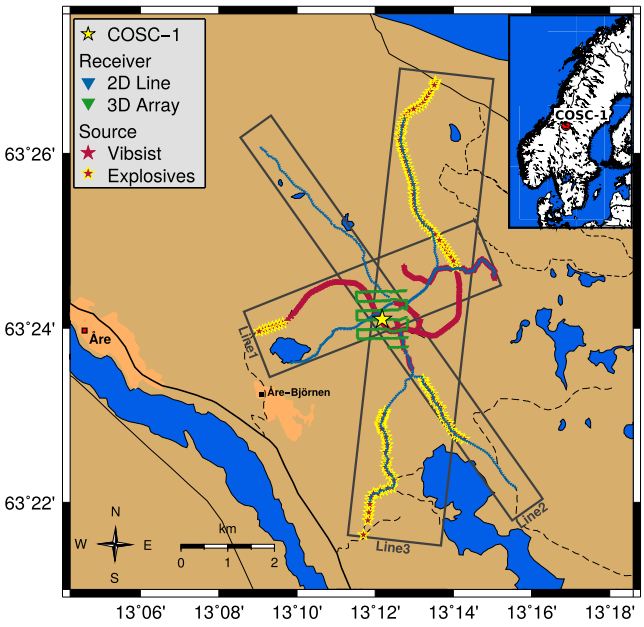

Figure 3. Seismic source (VIBSIST: red, Explosives: red with yellow fringe) and receiver lines (blue) for the multiazimuthal walkaway VSP and the long offset surface lines, centred around the COSC-1 borehole (yellow star). In the central part the 3-D receiver array (green) is shown, which recorded shots from the same source positions. Rectangles indicate the lateral extent of the 3-D models for the first-arrival tomographies.

(Hedin *et al.* 2012). This is probably due to the small-scale complex 3-D geometry and strong scattering of the seismic energy (Hedin 2015). In the eastern part of these profiles, the base of the nappes can be clearly identified for about 20 km at a depth of 0.5–1 km but then rapidly deepen just east of Åre. The influence of the Caledonian deformation on the underlying basement is less well defined (Gee 1978; Gee *et al.* 2010). Within the autochthonous basement (below the uppermost 1–2 km), the seismic data (CSP, CCT) show mainly northwest-dipping structures, which might represent dolerite intrusions (Juhojuntti *et al.* 2001) or deformation zones of Caledonian or pre-Caledonian age (Palm *et al.* 1991). Their definitive origin remains enigmatic without drilling into them.

1.3 New borehole based investigations

The COSC-1 borehole was drilled in 2014 near the town of Åre in western Jämtland (IGSN: ICDP5054EHW1001, Fig. 3) with nearly 100 per cent core recovery to a final depth of 2496 m (Lorenz *et al.* 2015b). The drilling was complemented by extensive logging measurements of geophysical and geochemical parameters on the core and in the borehole (Berthet *et al.* 2015; Lorenz *et al.* 2015a,b). Right after drilling, a major borehole based seismic survey was conducted in and around the COSC-1 borehole that comprised both seismic reflection and transmission experiments. The survey consisted of three parts: (1) a high resolution zero-offset Vertical Seismic Profile (VSP; Krauß *et al.* 2015), (2) a multiazimuthal walkaway VSP in combination with three long offset surface receiver lines (this study) and (3) a spatially limited 3-D seismic survey (Hedin *et al.* 2016). Combined with core analysis and downhole logging, the results of this survey will allow for the extrapolation of structures and petrophysical properties away from the borehole, and therefore define the characteristics of the SNC and further the understanding of the nappe emplacement processes. Additionally, the previously

Table 1. Acquisition source parameters for the multiazimuthal walkaway survey and the long offset surface lines.

	VIBSIST-3000	Explosives
Source points	508	128
Excitations per source point	4–5	1–2
Sweeps per excitation	3	–
Hit interval for hammer	100–200 ms	–
Sweep length	20 s	–
Source spacing	20 m	80 m
Explosive charge	–	0.5 kg
Explosive charge depth	–	3–5 m
Shothole filling	–	Water/gravel

Table 2. Acquisition receiver parameters for the multiazimuthal walkaway survey and the long offset surface lines.

	Surface receiver	Borehole receiver
Number of receivers	180	15
Receiver type	4.5 Hz, 3C	15 Hz, 3C
Receiver spacing	∼50 / ∼30 m	10 m
Offset (horizontal)	0–9054 m	25–5200 m
Recording instrument	Omnirecs DATA-CUBE3	Sercel Slimwave Geophone Chain
Sample rate	2.5 ms	1 ms
Record length	Continuous recording	25 s

mentioned limitations caused by the 2-D survey geometry of the CSP profile are also overcome by incorporating these new borehole based seismic investigations.

In order to produce reliable images of the structures around the borehole, an appropriate velocity model is needed, especially for the application of pre-stack depth migration methods. Except for the mentioned large scale refraction seismic investigations by Palm (1984), no studies have investigated the velocity distribution of the SNC. Therefore, this study presents the first velocity model of the SNC in the vicinity of the COSC-1 borehole, based on the combined evaluation of a unique VSP and surface seismic data set, acquired along different azimuths around the borehole. The comparison of velocities from mainly horizontally travelling waves (first-arrival tomography results) with mainly vertically travelling waves (derived from zero-offset VSP first-arrival traveltimes), provides evidence that the SNC is characterized by seismic anisotropy. We show that the isotropic traveltime tomography cannot explain first-arrival traveltimes from both borehole and surface seismic data at once. However, the traveltimes from all survey components can be well explained by an anisotropic VTI (transversely isotropic with vertical axis of symmetry) model, representing the SNC as a whole.

2 DATA ACQUISITION

After the COSC-1 borehole drilling was completed, a major seismic survey in and around the borehole was conducted in September and October 2014. The investigation consisted of three parts:

(i) The first survey part was a high resolution zero-offset Vertical Seismic Profile (VSP) (Krauß *et al.* 2015), using a borehole receiver chain with 15 three-component 15 Hz geophones. The borehole receiver chain was operated such that a final receiver interval of 2 m between 10 m and 2480 m drillers depth could be achieved. For this part of the survey, the source was located 30 m away from the wellhead of the borehole. The source was a rock breaking hydraulic hammer (VIBSIST-3000) mounted on a construction vehicle (Park *et al.* 1996; Cosma & Enescu 2001; Juhlin *et al.* 2010), which hit the ground repeatedly for 20 s with a decreasing hit interval of 100-200 ms. To generate seismograms for further processing, the recorded signals of this source type were decoded afterwards using the shift-and-stack method (Park *et al.* 1996).

(ii) The main focus of this paper lies in the second survey component, a multiazimuthal walkaway VSP in combination with 2-D long offset surface receiver lines. An overview of the acquisition parameters can be found in Table 1 for the sources and in Table 2 for the receivers.

For these experiments, the source points were distributed in a star pattern along three profile lines, which were up to 10 km long and centred around COSC-1 (see Fig. 3), resulting in a maximum distance of 5200 m from the borehole. Because of the forested and mountainous terrain, the profile lines are mostly bound to existing roads. For near offsets, up to 2.5 km distance to the drill site, the VIBSIST source was used. Each source position along the three profile lines was excited for several depth levels of the borehole chain (see Fig. 4), generating three sweeps per position. At source positions further than 2.5 km from the drill site, explosives in small shot holes (3.5–5 m depth) were fired twice. For the first shooting, the shot holes were filled with water to allow for a second usage. Because of damage to some of the holes, only 73 of the 128 shot holes could be used for a second time. When the shot holes where reused, they were filled with gravel to increase the emitted

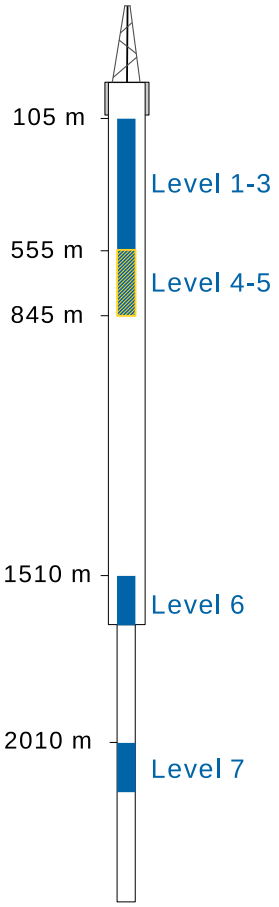

Figure 4. The borehole sketch showing the different depth levels of the borehole receiver array. Each level consists of 15 geophones with 10 m spacing. Explosive shots (far offset) were only recorded at level 4-5 (yellow fringe) and VIBSIST shots (near offset) were recorded at levels 1–3 and 6–7. The borehole was drilled down to 1616 m with H-size (96/63 mm hole/core diameter) and below with N-size (76/48 mm).

seismic energy. Source point spacing along the profile lines was approximately 20 m for the VIBSIST and 80 m for the explosive shots.

In the borehole, again a receiver chain with 15 three-component 15 Hz geophones at 10 m spacing was used and deployed at seven different depth levels during the survey. An overview of the borehole levels is shown in Fig. 4. The upper 5 levels, beginning directly below the installed borehole casing (open hole, except for the uppermost 102 m) at 105 m borehole depth, constitute a continuous section down to 845 m with 10 m receiver spacing. This depth interval was chosen in order to record diving waves in the borehole as well as at the surface on the opposite side of the profile. The determination of the crucial depth interval was done by raypath modelling, considering a range of expected velocity gradients. Level 6 (between 1510 and 1650 m borehole depth) and level 7 (between 2010 and 2150 m borehole depth), were chosen to constrain velocities in the deeper parts below the ray penetration depth for the surface recordings and to improve the depth resolution of imaging approaches. For each of the levels 1-3 and 6-7, VIBSIST shots from all shot positions were recorded (except for a small part of source line 3 for level 7), while the explosive shots were only recorded at levels 4–5.

On the surface, the wavefield was recorded by 180 wireless recorders equipped with three-component 4.5 Hz geophones placed along each of the three profiles (Fig. 3). The spacing between the receivers was 30 m for line 1 and 50 m for line 2 and line 3, resulting in a maximum source-receiver offset of about 6000 and 10 000 m, respectively.

Due to logistical constraints the receiver lines do not always coincide with the source positions. In some areas, small hiking paths and partly off-road areas were used to deploy the geophones preferably along straight lines. For technical and permitting reasons, some of these paths could not be used for the sources. This resulted in the partly different source and receiver line configuration, shown in Fig. 3.

(iii) The third part of the survey was a spatially limited 3-D surface seismic survey (Hedin *et al.* 2016), which consisted of 429 single-component geophones in a stationary spread at the central part around the COSC-1 borehole, covering an area of about 1.5 km^2 (see Fig. 3). This receiver array was active throughout most times of the multiazimuthal walkaway VSP experiment and recorded all source positions.

3 ISOTROPIC VELOCITY MODEL

3.1 First-arrival tomography

Seismic refraction traveltime analysis has long been a standard technique for imaging the subsurface, and a variety of traveltime tomography approaches have been developed during the last decades (Rawlinson & Sambridge 2003). These approaches differ mainly in terms of the ray-tracing approach used for the forward modelling or the regularization applied to the inverse problem. For example, with respect to the efficient computation of first-arrival traveltimes for the forward modelling, Vidale (1988) used a fast and simple ray-tracing approach by solving the eikonal equation with a finite-difference scheme. If the velocity contrast is large, this method violates a causality related to expanding a square wave front. A partial correction to this finite-difference solution was applied by Hole & Zelt (1995) on the basis of Fermat's principle. However, only a complete correction by expanding wave fronts with Huygens's principle can guarantee that the method converges to the global minimum in any complex model. This results in a more complicated and computationally expensive method.

For the inversion of first-arrival traveltimes we used the method developed by Zhang & Toksöz (1998), which consists of a shortest path ray-tracing approach (SPR) and a regularized nonlinear inversion method. In the SPR the seismic ray paths are found by calculating the shortest traveltime paths through a network of nodes, which is based on a graph template (e.g. Moser 1991). This includes the timing of the nodes along the expanding wave front, finding the minimum traveltime point along this wave front and expanding the wave front from this point. These steps are repeated until ray paths for the whole model are calculated. The wave front is therefore sampled with a uniform angle coverage. The regularized nonlinear inverse problem is solved by jointly minimizing the misfits of the average slowness (traveltime divided by ray length) and the apparent slowness (traveltime derivative with respect to distance). This leads to the inversion of traveltime curves instead of traveltimes alone. While the inversion of average slowness tends to reconstruct the shallow parts, the inversion of apparent slowness helps to reconstruct the deeper parts of the model (Zhang & Toksöz 1998). In order to constrain the model roughness, a second-order smoothing operator in the Tikhonov regularization, that numerically corresponds to a cubic spline interpolation, is applied in this approach. This leads to the objective function (Zhang & Toksöz 1998)

$$\begin{aligned}\Phi(m) &= (1-\omega)\|C_l(d-G(m))\|^2 + \omega\|D_x(d-G(m))\|^2 \\ &\quad + \tau\|Rm\|^2 \\ &= (1-\omega)\|\bar{d}-G(m)\|^2 + \omega\|\hat{d}-G(m)\|^2 \\ &\quad + \tau\|Rm\|^2, \end{aligned} \tag{1}$$

where d is the traveltime data, $G(m)$ is the calculated traveltime data for the current model m and C_l scales the traveltime with the corresponding ray length l, which gives the average slowness $\bar{d}$. D_x denotes the differential operator for the traveltime with respect to distance. Furthermore, $\hat{d} = D_x d$ returns the apparent slowness, R is the regularization operator, τ is a smoothing parameter and ω is a weighting factor between the average slowness misfit norm and the apparent slowness misfit norm. This function is minimized through the inversion process. The inversion is carried out using the Gauss–Newton method to linearize the stationary eq. (1) and then applying a conjugate gradient technique to solve the inversion for each iteration.

3.2 Velocity model building workflow

The derivation of velocity models from the long offset surface data and the multiazimuthal walkaway VSP data included several steps. In this section, the general workflow is explained in detail.

First, the first-arrival traveltimes were picked using an automatic picking routine. Due to the low signal-to-noise ratio, especially in case of the VIBSIST source and for longer offsets, the automatic picking routine failed for a substantial number of traces. Therefore, the picks had to be corrected manually. In the end, about 66 per cent of the surface data and 86 per cent of the borehole data first breaks could be identified and were used in the following inversions.

The first-arrival seismic tomography was carried out separately for each profile. Because of the crooked line geometry, a 3-D grid for every line was defined (see Fig. 3) with an equidistant grid spacing of 10 m in each direction. This gridded model was used for ray tracing during the tomography process. To reduce computational cost the grid spacing was increased to 20 m for the inversion.

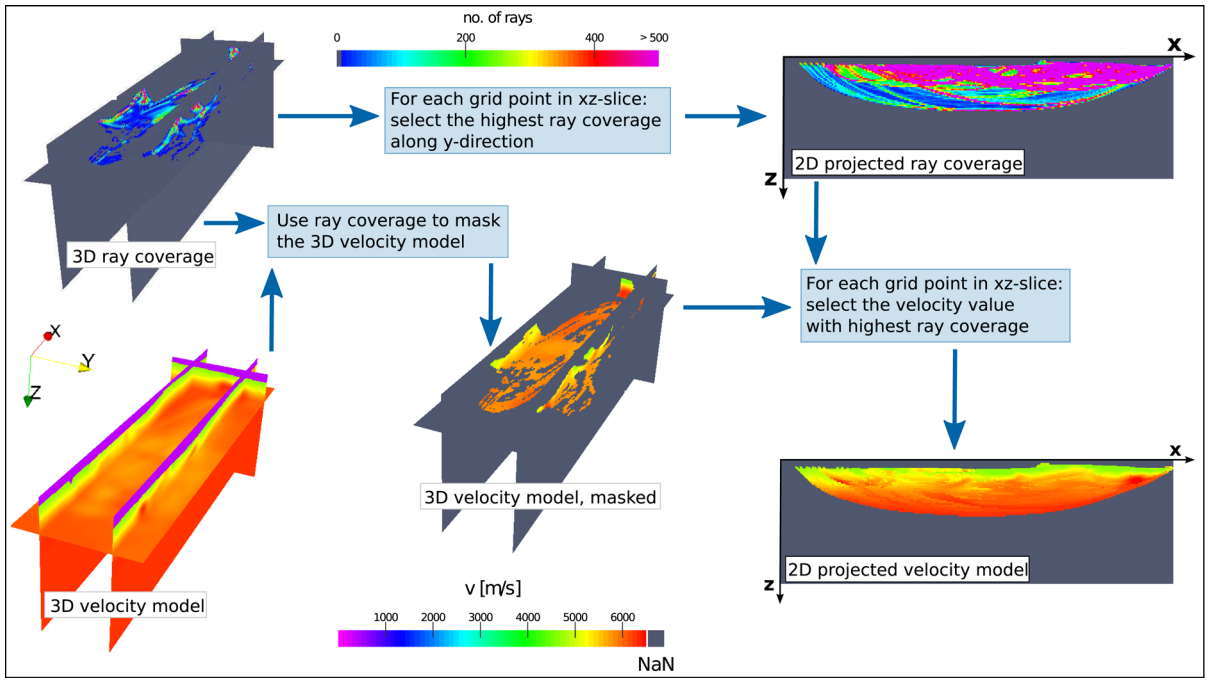

Figure 5. Conversion of the 3-D velocity model to the final 2-D velocity model based on the highest ray coverage.

All picked first-arrival traveltimes were plotted against their offset and refraction branches were identified, which defined the 1-D starting model. This 1-D model was then extended to three dimensions as a layered model with respect to surface topography. This pseudo 3-D starting model was updated iteratively in the 3-D inversion process until the root mean square (RMS) error indicated convergence. After testing different constant and adaptive smoothness constraints, we chose a constant medium smoothness constraint of $\tau = 2$ to be the most appropriate. The accuracy of the final velocity model was assessed by a low RMS value ($\ll$20 ms) and by visually comparing observed traveltimes in the data with the traveltimes computed from the inverted velocity model.

From the 3-D inversion output model, a representative 2-D velocity model was generated for each profile. This was achieved by masking those parts of the 3-D model that have zero ray coverage and therefore were not updated during the inversion. The ray coverage was assessed by performing a ray tracing for the final model and counting the number of rays penetrating each cell of the 3-D inversion grid. Afterwards, *xz*-slices of the inversion output model were stacked according to the highest ray coverage in each cell. That is, a single velocity value was assigned to each *xz* grid point according to the maximum ray density for all *y*-slices at this *xz* grid point. Fig. 5 illustrates this conversion from the 3-D inversion output model to the final 2-D model.

3.3 Traveltime inversion of surface data

As first step we only inverted the first-arrival traveltimes from sources and receivers distributed along the surface. Fig. 6 shows the resulting 2-D velocity models for each profile line. In general, the velocities increase with depth and all three lines show very few lateral velocity changes. Near the surface, the velocity is about 5000 m s^{-1}, except for the eastern part of line 1 and for two areas in the south-eastern part of line 2, where the velocity has lower values of about 4600 m s^{-1}. The 'ray-path shaped' velocity anomalies that occur in all models are artefacts caused by the conversion from a

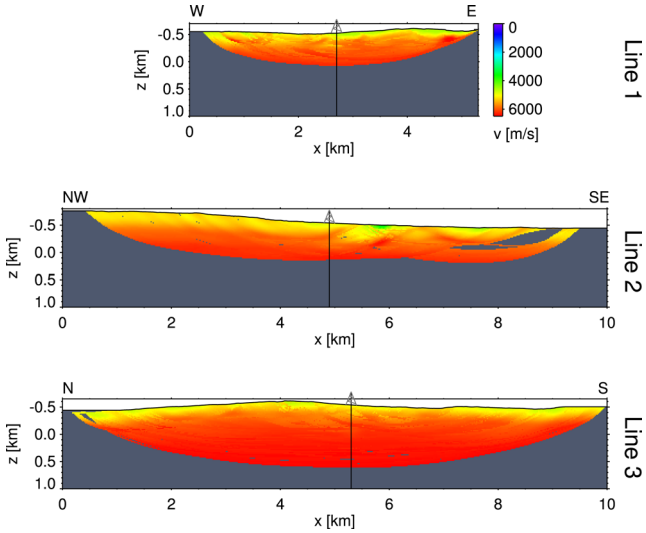

Figure 6. Results of 3-D first-arrival seismic tomography converted into 2-D slices for the three surface lines. Each profile was inverted separately. Parts with no ray coverage are masked. The colour scale next to the model of line 1 applies to all three models.

3-D volume to a 2-D slice. Nevertheless, the final 2-D image is a reasonable representation of the 3-D volume, because the most accurately calculated (in terms of ray coverage) velocity values for each cell were stitched together.

The maximum penetration depth of the diving waves defines the maximum depth up to which the traveltime inversion can provide information. Areas below the maximum penetration depth are masked, because of zero ray coverage. The depth of our models is therefore highly dependent on the velocity gradient and the maximum source-receiver offsets. Due to the shorter offsets of less than 5300 m, the model of line 1 has only velocity information down to 600 m depth, while the model of line 3 (maximum offset 10 000 m) provides values down to 1100 m depth.

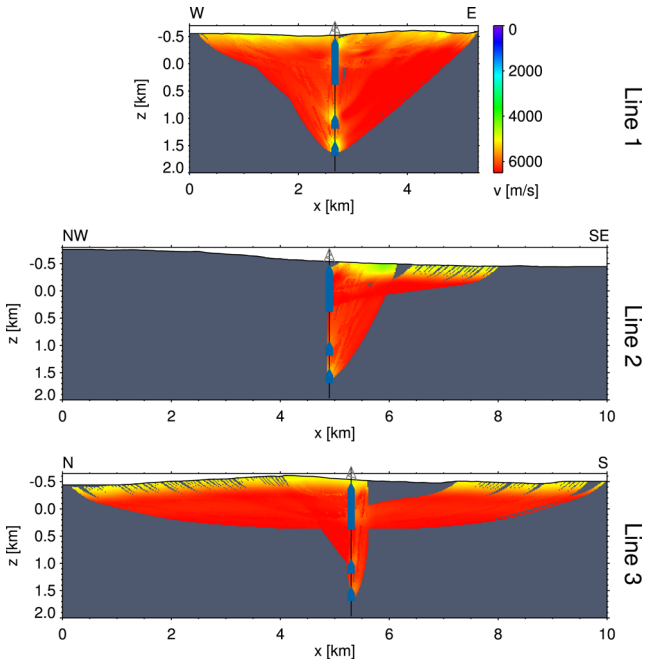

Figure 7. Results of 3-D first-arrival seismic tomography converted into 2-D slices using only first-arrival traveltimes recorded in the borehole. Each profile was inverted separately. Parts with no ray coverage are masked. The colour scale next to the model of line 1 applies to all three models. The positions of the borehole geophones are marked in blue.

No source positions were activated in the northern and southernmost part of line 2. Shot positions were located only at the central southern part of the profile (see Fig. 3). The tomography algorithm used here, only updated the parts of the model that are situated between the minimum and maximum shot positions. Hence, reliable velocity values could be obtained only for a very small part of the profile. As a workaround, we duplicated the data from this line and switched source and receiver positions assuming reciprocity of traveltimes. The inversion was then carried out with the duplicated (now common receiver gather sorted) data set. This resulted in a much more uniform ray coverage over the entire profile length and therefore in more parts of the model being updated during inversion.

The three independently inverted models show a good general agreement of the velocity gradient. In all three models, at a depth of 500 m below topography the velocity ranges between 6120 m s^{-1} and 6160 m s^{-1}. Below this depth the velocity gradient decreases and a velocity of about 6400 m s^{-1} is reached at the maximum penetration depth of approximately 1000 m in the model of line 3.

3.4 Traveltime inversion of borehole data

As a second step we incorporated the borehole data from the multiazimuthal walkaway VSP experiment, that is, we used the data recorded by the borehole geophone chain at the different depth levels. In this case, the sources were located along the profile lines at the surface and the waves travelled from the source to the receivers in the borehole. As a consequence, vertical travel paths dominate for shot positions near the borehole and more or less horizontal travel paths dominate for far offsets.

Fig. 7 shows the results of the inversion using only first-arrival traveltimes recorded in the borehole. Because of the specific survey geometry, the ray-path coverage is poor compared to surface seismic data, especially for lines 2 and 3. As mentioned above, the source positions of line 2 were only in the southeastern part of the profile and for all lines the shot points further away from the borehole (explosive shots, see Fig. 3) have larger source spacing (see Table 1) and were only recorded at levels 4 and 5 in the borehole (555–845 m depth, see Fig. 4). The advantage of using the borehole recordings for the inversion is that velocities down to a depth of 2150 m (depth of the lowermost borehole receiver) could be derived, at least for limited parts of the model near the borehole.

The velocities in the upper 1000 m are quite consistent with the models obtained from surface data. At greater depths, the velocities seem to be more or less constant with values of about 6200 m s^{-1}. However, in all three models we observe two low velocity zones at about 1500–1650 m and 2000–2150 m depth in the direct vicinity of the borehole, corresponding to depths of the receiver levels 6 and 7. The velocities in these zones show decreased values of approximately 5700 m s^{-1} and 5300 m s^{-1}, respectively, while the surrounding velocities are approximately 6200 m s^{-1}. The spatial correlation of the velocity anomalies and receiver positions suggests that theses anomalies are artefacts of the inversion process. Careful quality control of the data and inversion parameters imply that the anomalies are caused through a wrong assumption, in this case an isotropic velocity model. The presented borehole based inversion includes waves that travel preferably horizontally (greater horizontal offset than receiver depth) and waves that travel more or less vertically (for shot positions near the borehole). This causes numerical artefacts, in the case of an anisotropic velocity field, because the inversion algorithm used here cannot handle seismic anisotropy. The incapability of the algorithm leads to artificial layering of lower and higher velocities. A similar artefact can be seen in about 500 m depth of the inversion results from lines 1 and 3, where vertical rays from the source points near the borehole cross the approximately horizontal rays from the far offset shots at the borehole receivers. It is most likely that these areas represent artefacts produced by the inversion. The anisotropy as a probable cause of this feature will be discussed in more detail in the following chapters.

3.5 Traveltime inversion of surface and borehole data

In the final inversion step, we used all available information for the tomography and inverted jointly first-arrival traveltimes recorded at the surface and those recorded by the geophones in the borehole. Again, for each profile the first-arrival tomography was carried out separately and the results are shown in Fig. 8. With this combination we could use the advantages of both previous approaches, namely the uniform ray density in the upper parts of the model from the surface data and the deeper ray penetration in the borehole data.

The resulting models are in very good agreement with the models derived from using only surface data (Fig. 6) and only borehole data (Fig. 7). In the upper parts, the observed velocity distribution is effectively the same as in the surface models. Even the shallow low velocity zones identified at the surface of the eastern part of line 1 and the low velocities near the surface of line 2 are again visible to the same extent. These zones could not be identified as clearly in the models from the borehole data, because of the irregular ray density. In the deeper parts of the model similar velocities as in the models from the borehole data can be observed, including the assumed artefacts (low velocities at about 1500–1650 and 2000–2150 m depth) presumably due to the presence of anisotropy.

A 3-D view of the final tomography results for the three lines (the same as in Fig. 8) is displayed in Fig. 9. The three profile lines were centred around the borehole COSC-1 and they show a good

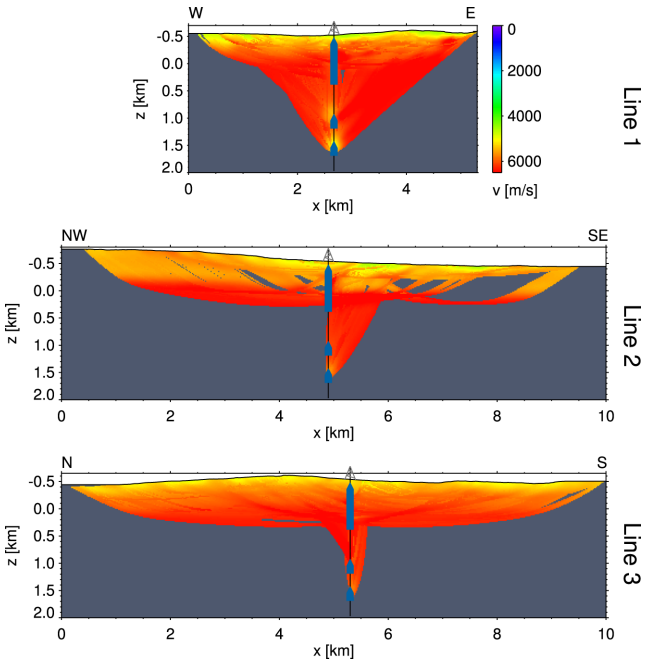

Figure 8. Results of 3-D first-arrival seismic tomography converted into 2-D slices using first-arrival traveltimes recorded in the borehole together with those recorded along the surface lines. Each profile was inverted separately. Parts with no ray coverage are masked. The colour scale next to the model of line 1 applies to all three models. The positions of the borehole geophones are marked in blue.

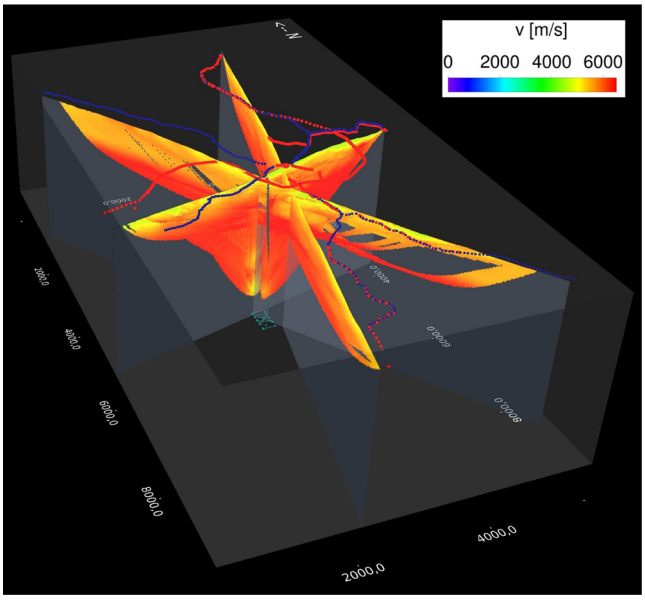

Figure 9. 3-D view of the results from first-arrival seismic tomography using first-arrival traveltimes recorded in the borehole together with those recorded along the surface lines (compare also Fig. 8), showing the good agreement between the three independently inverted models. Parts with no ray coverage are masked. The positions of the surface source and receiver positions are marked in red and blue, respectively.

agreement of the velocity values were they intersect each other, although they were inverted independently from each other.

3.6 Resolution and uncertainty of the tomographic models

Results based on tomography are non-unique. Therefore, a discussion of resolution and uncertainties is an important part when it comes to the assessment of tomographic models.

First of all, the uncertainty of the velocities obtained through the inversion procedure are highly dependent on the quality of the first-arrival picks. The first-arrival times were carefully picked and traces with unclear first breaks were left out. In order to measure the quality of the picks a reciprocal error was used. Because of reciprocity, the first-arrival traveltime from a point A to a point B should be equal to the traveltime from B to A. Due to picking errors, the difference between these traveltimes is not zero. For each shot the reciprocal shots within the receiver array was located and a RMS difference was calculated from the reciprocal traveltime differences. The average of this reciprocal error over all shots is 7.6 ms and the maximum error is 15.2 ms. Another quality control measure for the first break picks is the pick similarity. For two nearby shots, the traveltimes should be similar if they are projected on each other according to the offset. For well-picked shots, the RMS difference of traveltimes should be very small. For the data used here, this pick similarity was below 5 ms for every shot. We cannot expect the RMS error of the final model to be less than the error and uncertainty of the first-arrival traveltimes. The error caused by picking uncertainty mainly affects the apparent slowness $\hat{d}$ in eq. (1) and therefore this error tends to influence the uncertainty of deeper parts of the model (Zhang & Toksöz 1998).

The resolution of the tomographic model is mainly controlled by the width of the first Fresnel zone and therefore dependent on the wavelength of the signal. If we assume velocities between 4500 and 6000 m s^{-1} and frequencies between 10 and 15 Hz (dominant frequencies of the first-arrivals), we have minimum wavelengths between 300 and 600 m. For representative propagation distances of 1000 m and the above mentioned wavelengths, the width of the first Fresnel zone can be estimated as ∼500 m.

The ray distribution defines where and how well the model can be resolved. Therefore, we strictly masked those parts of the final model that could not be resolved at all, because of no rays crossing the corresponding inversion cells. The ray distribution is high (up to several hundred rays per cell) and uniform for the final models, because we stitched together those parts with the highest ray coverage (see Section 3.2).

3.7 Observed differences in vertical and horizontal velocities

From the zero-offset VSP data (Krauß *et al.* 2015), a velocity profile along the borehole was calculated by averaging the interval velocities, assuming a vertical borehole and therefore also vertical travel paths of the corresponding rays. This 1-D velocity profile is shown in Fig. 10(a). For comparison, velocities at the borehole location were extracted from the three different surface data tomography models (Fig. 6) and plotted in the same figure. The general trend of the velocities from the zero-offset VSP data shows an increasing velocity down to 1000 m depth. Below this depth the velocity is mainly constant. This generally correlates with the velocity trend from the tomography model at the borehole location, however the absolute values from the tomography are significantly higher. We assume that anisotropy present in the rocks causes this difference, because we are comparing velocities derived from mainly vertically travelling rays (zero-offset VSP) and mainly horizontally travelling rays (tomography using surface data). Showing line 3 as an example,

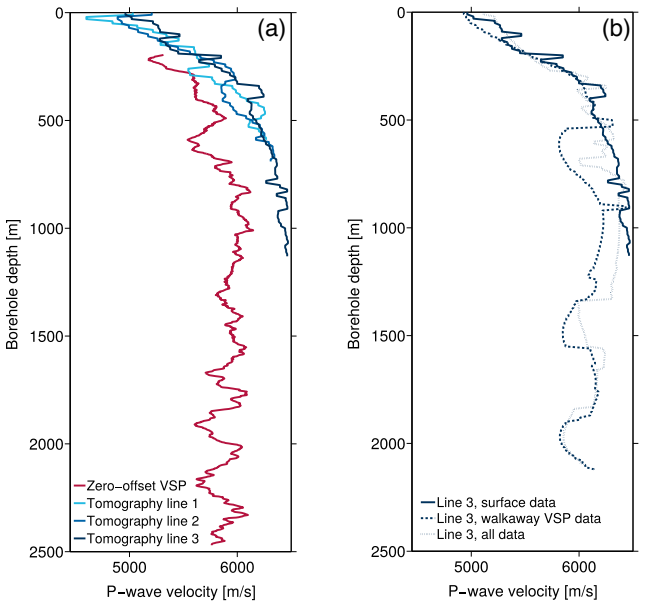

Figure 10. (a) Comparison of velocities at the borehole COSC-1 showing clear differences between velocities from zero-offset VSP (mainly vertically travelling rays) and from surface data tomography (mainly horizontally travelling rays). Velocity function from zero-offset VSP are calculated by averaging interval velocities and velocities from tomography are extracted from the 2-D images (Fig. 6) at the position of the borehole. (b) Comparison of velocity profiles (for line 3) from the different tomographic approaches, extracted from the 2-D images (Figs 6–8).

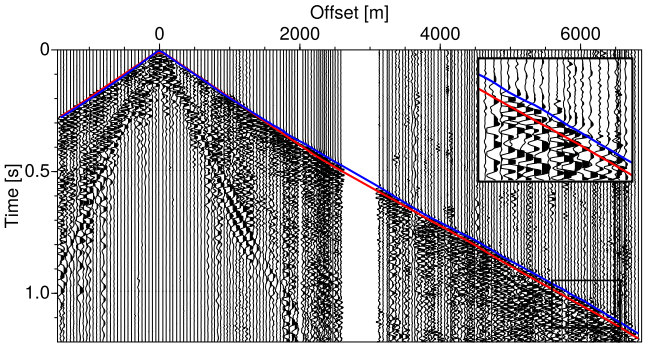

Figure 11. Shot gather from line 3 with calculated first-arrival traveltimes from the zero-offset velocity model (red) and from the tomography model calculated using only surface recordings (blue). While the first-arrival traveltimes calculated from the tomography velocity model fit the true observed first breaks very well, the first-arrival traveltimes calculated from the zero-offset velocity function yield in most of the cases late first-arrivals, especially for larger offsets.

Fig. 10(b) compares, the velocity profiles from the different tomographic approaches (Figs 6–8). There is a generally good agreement between the models down to a depth of 500 m. Below this depth the results from the walkaway VSP data inversion and the inversion of the combined data tend towards lower velocities and show the aforementioned strong artificial low velocity zones at 500, 1500 and 2000 m.

To further assess the models, we compared first-arrival traveltimes calculated from the tomography results and first-arrival traveltimes calculated from the 1-D velocity function derived from zero-offset VSP data with the observed first breaks picked in the shot gathers. Fig. 11 shows an example of a shot gather from line 3 with the calculated first-arrival traveltimes from the zero-offset velocity model plotted in red and from the tomography model calculated using only surface recordings plotted in blue. The first-arrival traveltimes calculated from the tomography velocity model fit the true first breaks very well. In contrast, the first-arrival traveltimes calculated from the zero-offset velocity function are typically too late, especially for larger offsets.

Fig. 12 shows a collection of example shot gathers from the borehole data with calculated first-arrival traveltimes from the zero-offset velocity model (red) and from the tomography model calculated using only surface recordings (blue). The left part (Figs 12a–c) shows shot gathers with increasing vertical source-receiver offset. Here the calculated first-arrival traveltimes from the zero-offet VSP model fit the data well, but the first-arrival traveltimes calculated from the tomography result are too early. In the right part (Figs 12d–f) shot gathers with increasing horizontal source-receiver offset are displayed, showing the first-arrival traveltimes calculated from the tomography results provide a good fit, but first-arrival traveltimes calculated from the zero-offset VSP velocity model are too late.

On the one hand, the tomography results provide a good fit to the first-arrival traveltimes in the surface data (see Fig. 11, blue line) and for far offset borehole data (see Figs 12e and f, blue lines). The latter is due to rays being closer to horizontal at far (horizontal) offsets between the source position and the borehole. In contrast, the calculated first-arrival traveltimes from the tomography are too early for the borehole data that have source positions near the borehole (Figs 12a–c). This effect becomes dominant for deeper borehole receivers and therefore longer travel paths. For example, Fig. 12(c) shows a difference between the calculated and real first-arrival traveltimes of more than 20 ms for a (vertical) travel path of about 2000 m.

On the other hand, the model derived from the zero-offset VSP data provide, as expected, a good fit of the first-arrivals in the near offset borehole data (Figs 12a–c, red lines). However, the first-arrival traveltimes calculated from this model for the surface data (see Fig. 11, red line) and far offset borehole data (Figs 12d–f) are late, corresponding to too low velocities. This effect becomes again more dominant for larger horizontal offsets between the borehole and source position. While the difference between the calculated and observed first-arrival traveltimes for an offset of 1000 m is about 10 ms (Fig. 12d), it is more than 30 ms for an offset of 2500 m (Fig. 12f).

It is therefore apparent that an isotropic velocity model cannot explain traveltimes at the surface and in the borehole. The observed differences in vertical and horizontal velocity provide clear evidence for seismic anisotropy around the borehole. It is not possible to simultaneously fit the surface data and zero-offset data with an isotropic velocity model. Thus, an anisotropic model that defines varying velocities for different travel path directions is required. In the following section such an anisotropic velocity model is introduced.

4 ANISOTROPIC VELOCITY MODEL

We constructed a VTI model, which is defined by three parameters: the vertical P-wave velocity $V_P(0)$ and the two Thomsen parameters ϵ and δ (Thomsen 1986). The following equations link the Thomsen parameters ϵ and δ to the horizontal P-wave velocity $V_P(\frac{\pi}{2})$, the vertical P-wave velocity $V_P(0)$ and the normal moveout (NMO) P-wave velocity $V_{\mathrm{NMO},P}$. While eq. (2), given by Thomsen (1986), is only valid under the assumption of weak anisotropy

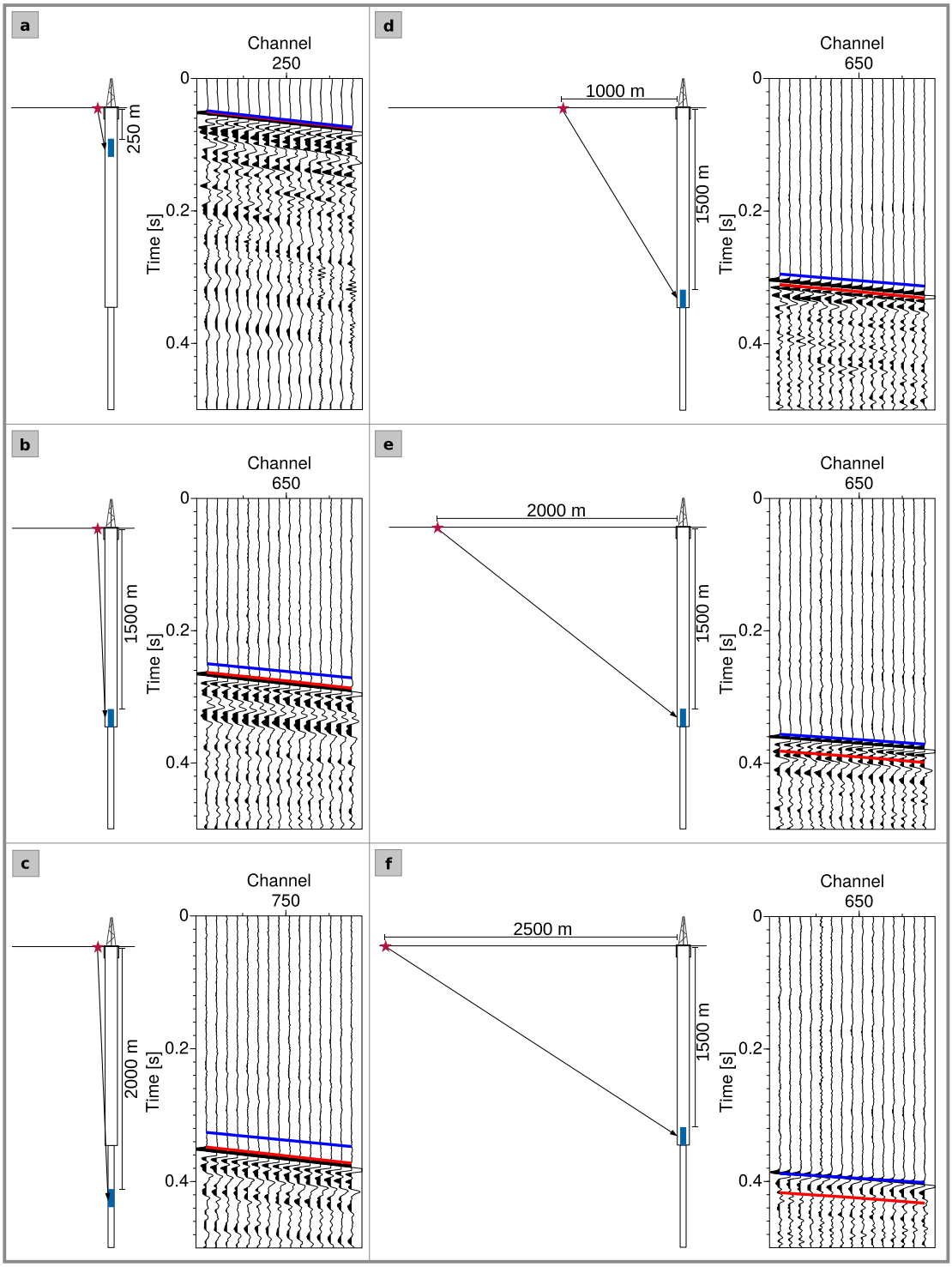

Figure 12. Shot gathers from borehole data with calculated first-arrival traveltimes for the zero-offset velocity model (red) and from tomography using only surface recordings (blue). (a–c) Increasing vertical source-receiver offset showing a good fit to the calculated first-arrivals from the zero-offset VSP model, but too early first-arrivals calculated from the tomography result. (d–f) Increasing horizontal source-receiver offset, showing a good fit with the first-arrivals calculated from the tomography results, but late first-arrivals calculated from the zero-offset VSP velocity model.

($|\epsilon| \ll 1$, $|\delta| \ll 1$), the eq. (3) by Tsvankin (2001) holds for anisotropy of arbitrary strength.

$$\epsilon = \frac{V_P(\frac{\pi}{2}) - V_P(0)}{V_P(0)} \tag{2}$$

$$V_{\mathrm{NMO},P} = V_P(0)\sqrt{1+2\delta}. \tag{3}$$

Fig. 13 together with the eqs (2) and (3) describe the general function of the three parameters and their influence on the traveltime isochrones in a VTI media corresponding to our survey geometry with sources at the surface and receivers on the surface as well as in the borehole. The vertical *P*-wave velocity directly influences the vertical traveltimes, that is, the traveltimes observed in the

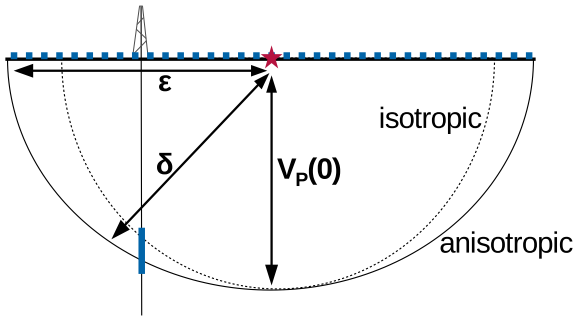

Figure 13. Sketch of the parameters used for the anisotropic model influencing the traveltime isochrones. While the vertical velocity $V_P(0)$ directly influences the vertical traveltimes, the Thomsen parameters ϵ and δ characterize the horizontally travelling waves and the steeper travelling waves, respectively. Therefore, the influence of ϵ can be seen directly in first-arrival traveltimes from surface data and the influence of δ in the far offset borehole data.

zero-offset VSP data. The parameter ϵ describes the ratio between the horizontal and vertical velocity and therefore characterizes the horizontally travelling waves. Consequently the effect of this parameter is directly visible in the first-arrival traveltimes of the surface data, in particular for large offset surface data. The second Thomsen parameter δ governs the normal moveout P-wave velocity $v_{\mathrm{NMO},P}$ in surface seismic data. Thus, it influences those parts of the traveltime isochrone that are neither vertical nor horizontal. Because of the survey geometry, the influence of δ can be directly observed in the first-arrival traveltimes of the far offset VSP data.

Following this VTI model description, the strategy for constructing the anisotropic model was consequently as follows: (1) find a velocity function that provides good fit to (near) zero-offset VSP first-arrival traveltimes, (2) fit the first-arrival traveltimes of the surface data by the parameter ϵ, (3) use the parameter δ to fit the first-arrival traveltimes of the far offset VSP data.

The 1-D velocity function used as the vertical velocity $V_P(0)$ was directly computed from the zero-offset VSP data by averaging the interval velocities. Therefore, we assumed a straight vertical borehole with the source directly at the wellhead and consequently vertical travelling waves. This velocity function is shown in Fig. 10(a). For the derivation of the Thomsen parameter ϵ we relied on information from borehole lithology and laboratory measurements. Following the description of the COSC-1 drill core by Lorenz *et al.* (2015b) the most common rock types are a succession of felsic, amphibole, calc-silicate gneisses, amphibolites and metagabbros down to 1700 m depth. Underneath, increasingly thick layers of mica-rich mylonites begin to appear (see Fig. 2) and become the most dominant rock type below 2100 m. Wenning *et al.* (2016) investigated seismic velocities and elastic anisotropy by ultrasonic laboratory measurements on selected core samples representing the lithology. In addition to the dynamic elastic moduli they also provide values for the Thomsen parameter ϵ. We choose the calc-silicate gneiss sample from 792.5 m depth as a representative for the dominating rock type in the upper 1700 m. For this sample, Wenning (2015) calculated a Thomsen parameter value of $\epsilon = 0.03$.

For the second Thomsen parameter δ, we performed several tests with a range of values by analysing the corresponding fit of the far offset VSP traveltimes, resulting in a final value of $\delta = 0.3$. These homogeneous values of ϵ and δ were used to set up an anisotropic VTI velocity model around the borehole.

The resulting VTI velocity model is shown in Fig. 14. For a source located at the surface traveltimes were computed for this anisotropic

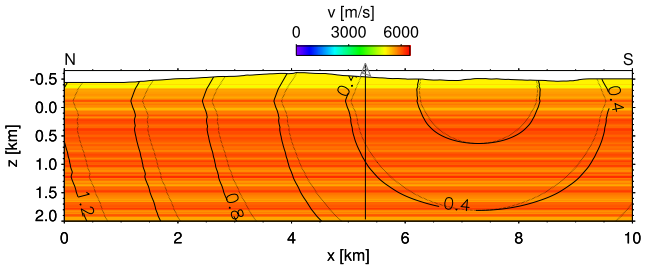

Figure 14. Anisotropic (solid) and isotropic (dotted) traveltime [s] isochrones along line 3 for one shot position. For the isotropic traveltimes the vertical velocities in the background are used. The anisotropic velocities were calculated using an anisotropic eikonal solver and the homogeneous Thomsen parameters $\epsilon = 0.03$ and $\delta = 0.3$.

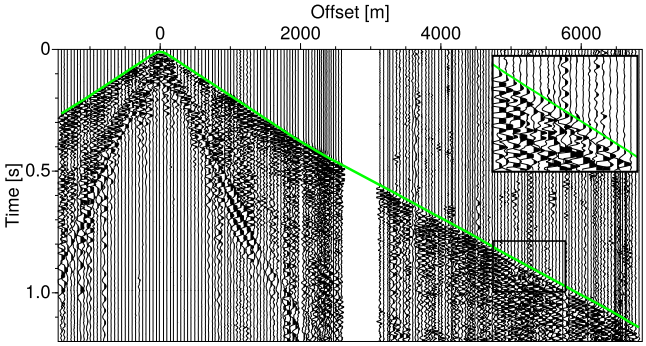

Figure 15. Shot gather from surface line 3 (the same shot as in Fig. 11), which shows very good agreement of the anisotropic model with surface seismic data. The green line shows the first-arrival traveltimes, calculated from the anisotropic velocity model using the vertical velocities from the zero-offset VSP and Thomsen parameters of $\epsilon = 0.03$ and $\delta = 0.3$.

model using an anisotropic eikonal solver (Riedel 2016). The resulting traveltimes are compared in Fig. 14 to traveltimes computed for the corresponding isotropic model with the same vertical velocity function but $\epsilon = \delta = 0$. As expected, the vertical traveltimes for both models coincide perfectly below the source position but differ significantly for other directions and larger offsets.

Fig. 15 shows the same shot gather as in Fig. 11, but now with the traveltimes calculated with the derived anisotropic model. In comparison to the isotropic models, the resulting anisotropic traveltimes now fit very well to the first breaks for both near and far offsets.

In Fig. 16, a similar comparison is presented for the same borehole shot gather shown in Fig. 12(e). Again, the derived anisotropic velocity model yields traveltimes that fit the first breaks very well.

5 DISCUSSION

In the following discussion we assess the validity of the different obtained velocity models and speculate about the geological causes for some of their features, for example the vertical velocity gradient and the lower velocity zones directly below the surface found in some of the tomographic models.

5.1 Tomographic models

The tomographic models show overall high P-wave velocities between 5000 and 6200 m s^{-1}, which are typical for the expected crystalline lithology of the SNC, consisting of gneisses, amphibolites and metagabbros. Even near the surface, the velocity values are in most parts higher than 5000 m s^{-1} which indicates that bedrock

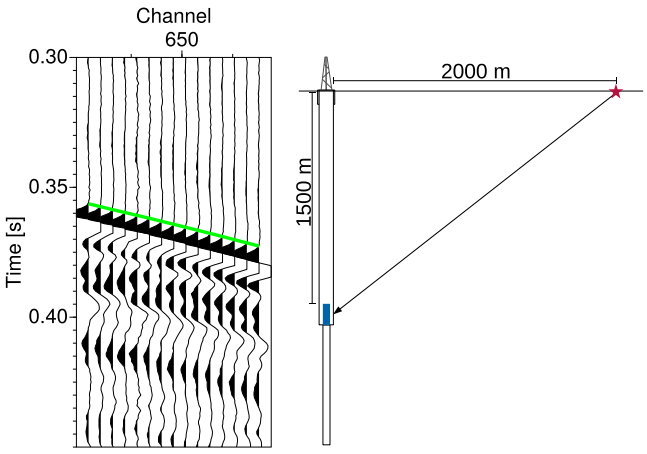

Figure 16. Shot gather from borehole data (the same shot as Fig. 12e, but with different time scaling) with calculated first-arrival traveltimes from the anisotropic velocity model using the vertical velocities from the zero-offset VSP and Thomsen parameters of $\epsilon = 0.03$ and $\delta = 0.3$, showing a very good fit to the observed first breaks.

Table 3. RMS misfit for all profile lines for each tomographic model, the anisotropic model and a model build from the 1-D zero-offset VSP velocity function.

RMS misfit [ms] of velocity model	Line 1	Line	Line 3
Tomography surface data	11.2	14.0	13.1
Tomography borehole data	10.5	10.1	10.3
Tomography surface and borehole data	11.1	13.4	12.5
Anisotropic model	10.8	12.7	11.1
1-D zero-offset VSP velocity function	21.6	24.7	23.4

occurs directly below the surface. We observe lower *P*-wave velocities of about 4600 m s^{-1} in the uppermost approximately 100 m of the eastern part of line 1 and south-eastern part of line 2. The reason for such values is unknown, but may be due to increased weathering of the rocks in this area.

Generally, all models are well resolved based on the high and uniformly distributed ray coverage. There are only some parts within the models that might have a lower resolution because there are fewer rays crossing each other. This is the case for the deeper parts of the models, where only waves, that originate from a source point near the borehole and that are recorded at the deep levels in the borehole pass through. The RMS misfit of the tomographic models is between 10–14 ms (see Table 3) and hence it lies within the range of the picking uncertainties (compare Section 3.6). For that reason at least the first-arrivals could be well explained by all models. However, for the models which also include the borehole data, artificial low velocity zones near the borehole receivers occur (see Figs 7 and 8). The models which result from using only surface receivers and correspondingly mainly horizontal ray paths, give the most reliable estimate of the horizontal propagation velocity, while the 1-D velocity model from the zero-offset VSP (see Fig. 10a) yields the most reliable results for the vertical propagation velocity. The 1-D zero-offset VSP velocity profile does not provide a robust estimate for the area, based on its comparably bad RMS misfit of more than 20 ms (see also Table 3).

5.2 Vertical velocity gradient

A relatively strong vertical velocity gradient can be observed in both the tomographic models and in the interval velocities from the zero-offset VSP. This may have several reasons. The closing of micro-cracks and fractures with increasing depth influences the density and elastic moduli of the rocks and therefore could cause such a velocity gradient. Palm (1984) also found a continuously increasing velocity with depth in all rocks in the area, which he relates mainly to the decreasing width and frequency of fractures. Under a certain pressure and at a certain depth, all cracks are closed and the density and elastic moduli do not increase further. In our case this condition is probably observed at a depth of about 1000 m, since the velocity seems to be more or less constant at greater depths, with values of about 6200 m s^{-1} in the tomographic models and about 6000 m s^{-1} in the interval velocities from zero-offset VSP.

Furthermore, the lithology affects the velocities, since the amount of mafic rocks (amphibolites, metagabbros) slightly increases with depth. According to Hedin *et al.* (2016), the *in situ* downhole density and *P*-wave velocity logs reveal a higher average density (3000 kg m^{-3}) and *P*-wave velocity (6000 m s^{-1}) for the mafic rocks compared to the dominant felsic gneisses (2800 kg m^{-3}, 5700 m s^{-1}).

Also, the occurrence of anisotropy might influence the velocity gradient, at least to a small amount. Even for those models where only surface receiver were used, that is, mainly horizontally travelling rays, a small part of the ray paths near the surface are still vertical, especially for large offsets. Since the vertical velocity is comparably lower than the horizontal velocity, these vertical ray paths could cause lower velocity near the surface. The control of vertical ray paths with depth decreases because of the ray paths are more horizontal, and therefore the velocity increases.

Comparable velocity gradients in crystalline environments are rare, but can be found for example for gneisses in the area of the KTB (German Continental Deep Drilling Programme) in south-eastern Germany. Here, the interval velocity profiles deduced from sonic and VSP measurements show an even stronger velocity gradient for gneisses in the uppermost 1000 m of the KTB borehole (Lüschen *et al.* 1996). Another example can be found in Alberta (Canada) where the interval velocities from VSP measurements reveal an increasing velocity with depth from approximately 5500 to 6500 m s^{-1} for the crystalline basement rocks (granitoids, gneisses, metasediments) of the Canadian Shield (Chan & Schmitt 2015). For this reason we conclude that the observed vertical gradient is a reasonable estimate for the area, even if slightly overestimated due to the anisotropy.

5.3 Anisotropic VTI model

The anisotropic model yields a very good fit of the first-arrival traveltimes, although it is a simplified approximation using a 1-D vertical velocity function and homogeneous Thomsen parameters. The overall RMS misfit for the anisotropic model is 11.5 ms (Table 3), taking into account all first-arrival times from surface and borehole data along all three lines. It is comparable and even slightly lower than most of the RMS values for the tomographic models.

Fig. 17 shows the first break pick times from all shot gathers plotted against the absolute source-receiver offset. Since the horizontal offset is plotted, the picks from the borehole data show an initial time delay gap, depending on their depth level and the corresponding vertical source-receiver offset of up to 0.35 s. Hence, they do not appear within the linear trend of the first breaks from the surface and the far offset borehole data. In addition to the first break

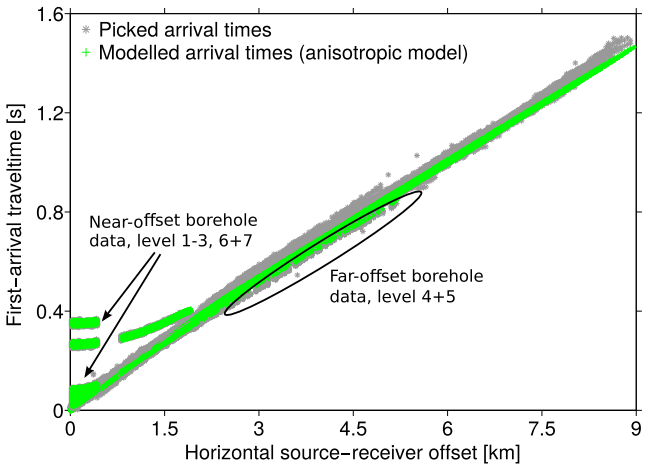

Figure 17. Plot of the first break pick times from all shot gathers against the absolute source-receiver offset. On top of the first break pick times, the corresponding first-arrival times calculated from the anisotropic velocity model are displayed. The near-offset borehole data picks show an initial time delay gap, which is due to their vertical source-receiver offset.

picks, the corresponding first-arrival traveltimes, calculated from the anisotropic velocity model are displayed, showing in general a good agreement between the observed and modelled traveltimes.

The use of a VTI as a first estimation is also justified by the geological setting, since the layering of the Seve Nappes in this area is on average more or less horizontal with some structures dipping only slightly in different directions (Hedin *et al.* 2016). Moreover, also the COSC-1 core has, at least on the sample-scale, a pseudo-vertically transverse isotropic (VTI) behaviour and the tectonic foliation generally dips only shallowly in alternating directions (Wenning *et al.* 2016). The ϵ value from the calc-silicate gneiss sample that was derived from laboratory measurements could be verified by the data from the surface seismic experiment. Several other values in the range $\epsilon = 0.01$–0.1 were tested. A deviation as small as ± 0.015 from the used value ($\epsilon = 0.03$) resulted in an increasing RMS error of about 2 ms. Therefore, it seems to be a reasonable estimate of the *P*-wave anisotropy of the Seve Nappes in the survey area. This is certainly true if we look at the Seve Nappes on a larger scale. There may be local parts that have much higher ϵ values, for example in the mica-bearing mylonite zones below 2100 m depth (Lorenz *et al.* 2015b). Unfortunately no δ values could be derived from the ultrasonic laboratory measurements (Wenning *et al.* 2016). Therefore, we had to completely rely on the seismic measurements, in particular the far offset VSP data. Again, the value of δ which we obtained is an average over the Seve Nappes as a whole in the COSC-1 area. Nevertheless, it seems to be a reasonable value, because it fits the first breaks of the seismic data very well. Despite the mentioned limitations, the anisotropic model is a far better estimate of the velocity distribution around the borehole COSC-1 than the isotropic model, since it accounts for varying velocities in different travel path directions. It is therefore the only velocity model that explains the first-arrival times of all survey components at once.

6 SUMMARY AND CONCLUSIONS

Within the project COSC, two approximately 2.5 km deep fully cored boreholes will be drilled through the allochthonous units of the Scandinavian orogen and the underlying Precambrian crystalline basement in order to examine the structure and physical conditions. The first borehole COSC-1 was successfully drilled in 2014. It sampled a thick section of the lower unit of the high metamorphic grade SNC, which constitutes the uppermost part of the Middle Allochthon and originates from the outermost margin of the Baltica palaeocontinent.

Borehole based seismic investigations including zero-offset VSP, multiazimuthal walkaway VSP, long offset surface lines, and a limited 3-D survey took place right after drilling. From the long offset surface lines in combination with the multiazimuthal walkaway VSP data, isotropic velocity models could be derived for different azimuths around the borehole by using a 3-D first-arrival seismic tomography approach. Clear evidence for anisotropy was found by comparing the first-arrival traveltimes calculated from velocity models using only vertical ray paths (zero-offset VSP) and models using mainly horizontally travelling waves (tomography). Consequently, clear differences between horizontal (fast) and vertical (slow) velocities were observed, which made the construction of an anisotropic velocity model necessary. The constructed VTI anisotropic model consists of a 1-D vertical velocity function calculated directly from the zero-offset VSP first-arrivals and the homogeneous Thomsen parameters $\epsilon = 0.03$ and $\delta = 0.3$. The latter were partly derived from laboratory measurements and the seismic walkaway VSP data. With this relatively simple anisotropic model, first-arrival traveltimes for both surface and borehole data can be very well explained simultaneously.

Traveltimes calculated from the anisotropic model can serve as the basis for the application of imaging approaches like pre-stack depth migration techniques. This may lead to high-resolution images of the fine-scale structures around the borehole, which is vital information for the reliable spatial extrapolation of the structures and petrophysical properties observed in the borehole into the surrounding rock formations, especially the SNC. Hence, this will strengthen the understanding of the tectonic and geodynamic setting, including but not limited to, the past and present stress regime.

ACKNOWLEDGEMENTS

We thank the German Research Foundation (DFG, grants BU1364/10-1 and GI982/2-1) for funding the VSP component of the survey within the Priority Program ICDP (SPP 1006). The Geophysical Instruments Pool Potsdam (GIPP) provided the surface geophones and wireless recorders (Cubes) for the multiazimuthal walkaway VSP experiment. Hans Palm (HasSeis) extensively helped with the planning, permitting and accomplishment of the survey. We thank the field crew members Konstanze Zschoke, Christin Mann, Svenja Schotte, Christine Seupel, Sebastian Buntin, Sandro John, Olaf Hellwig, Felix Hloušek (students and staff from TU Bergakademie Freiberg), Monika Ivandic, Fei Huang, Fengjiao Zhang (Uppsala University), Andreas Jurczyk, Kay Krüger (GFZ Potsdam), Jochem Kück, Martin Töpfer (ICDP Operational Support Group) and Fabienne Reiser (ETH Zurich) for their hard work in the field. We are particularly grateful to the reviewers and the editor for their thorough and constructive comments which helped to improve the paper.

REFERENCES

Andersen, T.B., 1998. Extensional tectonics in the Caledonides of southern Norway, an overview, *Tectonophysics,* **285,** 333–351.

Andréasson, P.G., 1994. The Baltoscandian margin in Neoproterozoic-early Palaeozoic times. Some constraints on terrane derivation and accretion in the Arctic Scandinavian Caledonides, *Tectonophysics,* **231,** 1–32.

Berthet, T., Alm, P.-G., Wenning, Q., Almqvist, B.S., Kück, J. & Hedin, P., 2015. Borehole logging at the COSC-1 drill hole: a new dataset of in-situ geophysical properties through the lower Seve Nappe Complex, *Geophys. Res. Abstr.,* **17,** EGU–15475.

Chan, J. & Schmitt, D.R., 2015. Initial seismic observations from a deep borehole drilled into the Canadian Shield in northeast Alberta, *Int. J. Earth Sci.,* **104**(6), 1549–1562.

Corfu, F., Gasser, D. & Chew, D.M. (eds), 2014. *New Perspectives on the Caledonides of Scandinavia and Related Areas*, Geological Society, London, Special Publications 390, doi:10.1144/SP390.28.

Cosma, C. & Enescu, N., 2001. Characterization of fractured rock in the vicinity of tunnels by the swept impact seismic technique, *Int. J. Rock Mech. Min. Sci.,* **38**(6), 815–821.

Dyrelius, D., 1985. A geophysical perspective of the Scandinavian Caledonides, in *The Caledonide Orogen - Scandinavia and Related Areas,* pp. 185–194, eds Gee, D.G. & Sturt, B.A., John Wiley & Sons.

Dyrelius, D., 1986. Gravity and magnetics in the central Scandes, *Geol. Foereningan i Stock. Foerhandlingar,* **108**(3), 278–280.

Dyrelius, D., Gee, D., Gorbatschev, R., Ramberg, H. & Zachrisson, E., 1980. A profile through the central scandinavian caledonides, *Tectonophysics,* **69**(3–4), 247–284.

Ebbing, J., England, R., Korja, T., Lauritsen, T., Olesen, O., Stratford, W. & Weidle, C., 2012. Structure of the Scandes lithosphere from surface to depth, *Tectonophysics,* **536–537,** 1–24.

Elming, S.A., 1988. Geological modelling based on gravity data from the central part of the Swedish Caledonides, *Geol. Föreningen i Stock. Förhandlingar,* **110**(4), 317–327.

England, R.W. & Ebbing, J., 2012. Crustal structure of central Norway and Sweden from integrated modelling of teleseismic receiver functions and the gravity anomaly, *Geophys. J. Int.,* **191**(1), 1–11.

Gee, D.G., 1975. A Tectonic Model For Central Part of Scandinavian Caledonides, *Am. J. Sci.,* **275-A,** 468–515.

Gee, D.G., 1978. Nappe Displacement In Scandinavian Caledonides, *Tectonophysics,* **47**(3–4), 393–419.

Gee, D.G. & Sturt, B.A. eds, 1985. *The Caledonide Orogen - Scandinavia and Related Areas,* John Wiley & Sons Ltd.

Gee, D.G., Fossen, H., Henriksen, N. & Higgins, A.K., 2008. From the early Paleozoic platforms of Baltica and Laurentia to the Caledonide orogen of Scandinavia and Greenland, *Episodes,* **31**(1), 44–51.

Gee, D.G., Juhlin, C., Pascal, C. & Robinson, P., 2010. Collisional Orogeny in the Scandinavian Caledonides (COSC), *Geol. Föreningen i Stock. Förhandlingar,* **132**(1), 29–44.

Grimmer, J.C., Glodny, J., Druppel, K., Greiling, R.O. & Kontny, A., 2015. Early- to mid-Silurian extrusion wedge tectonics in the central Scandinavian Caledonides, *Geology,* **43**(4), 347–350.

Hedin, P., 2015. Geophysical studies of the upper crust of the central Swedish Caledonides in relation to the COSC scientific drilling project, *PhD thesis,* Uppsala University.

Hedin, P., Juhlin, C. & Gee, D.G., 2012. Seismic imaging of the Scandinavian Caledonides to define ICDP drilling sites, *Tectonophysics,* **554–557,** 30–41.

Hedin, P., Malehmir, A., Gee, D.G., Juhlin, C. & Dyrelius, D., 2014. 3D Interpretation by integrating seismic and potential field data in the vicinity of the proposed COSC-1 drill site, central swedish Caledonides, in *New Perspectives on the Caledonides and Related Areas,* pp. 301–319, eds Corfu, F., Gasser, D. & Chew, D., *Geological Society*, London, Special Publications 390.

Hedin, P. *et al.*, 2016. 3D reflection seismic imaging at the 2.5 km deep COSC-1 scientific borehole, central Scandinavian Caledonides, *Tectonophysics,* **689,** 40–55.

Hole, J.A. & Zelt, C.A., 1995. 3-D finite-difference reflection travel times, *Geophys. J. Int.,* **121**(2), 427–434.

Hurich, C.A., Palm, H., Dyrelius, D. & Kristoffersen, Y., 1989. Deformation of the Baltic continental crust during Caledonide intracontinental subduction: views from seismic reflection data, *Geology,* **17**(5), 423, doi:10.1130/0091-7613(1989)017<0423:DOTBCC>2.3.CO;2.

Juhlin, C., Dehghannejad, M., Lund, B., Malehmir, A. & Pratt, G., 2010. Reflection seismic imaging of the end-glacial Pärvie Fault system, northern Sweden, *J. Appl. Geophys.,* **70**(4), 307–316.

Juhlin, C., Hedin, P., Gee, D.G., Lorenz, H., Kalscheuer, T. & Yan, P., 2016. Seismic imaging in the eastern Scandinavian Caledonides: Siting the 2.5 km deep COSC-2 borehole, central Sweden, *Solid Earth,* **7,** 769–787.

Juhojuntti, N., Juhlin, C. & Dyrelius, D., 2001. Crustal reflectivity underneath the Central Scandinavian Caledonides, *Tectonophysics,* **334**(3–4), 191–210.

Klonowska, I., Majka, J., Janak, M., Gee, D.G. & Ladenberger, A., 2014. Pressure-temperature evolution of a kyanite–garnet pelitic gneiss from Areskutan: evidence of ultra-high-pressure metamorphism of the Seve Nappe Complex, west-central Jamtland, Swedish Caledonides, in *New Perspectives on the Caledonides and Related Areas,* pp. 321–336, eds Corfu, F., Gasser, D. & Chew, D., Geological Society, London, Special Publications 390, doi:10.1144/SP390.7.

Klonowska, I., Janak, M., Majka, J., Froitzheim, N. & Gee, D.G., 2015. Discovery of microdiamond in the Åreskutan Nappe of the Seve Nappe Complex, overlying the COSC-1 drillhole, *Geophys. Res. Abstr.,* **17,** EGU–12046.

Korja, T., Smirnov, M., Pedersen, L.B. & Gharibi, M., 2008. Structure of the Central Scandinavian Caledonides and the underlying Precambrian basement, new constraints from magnetotellurics, *Geophys. J. Int.,* **175**(1), 55–69.

Krauß, F., Simon, H., Giese, R., Buske, S., Hedin, P., Juhlin, C. & Lorenz, H., 2015. Zero-Offset VSP in the COSC-1 borehole, *Geophys. Res. Abstr.,* **17,** EGU–3255.

Ladenberger, A., Be'eri-Shlevin, Y., Claesson, S., Gee, D.G., Majka, J. & Romanova, I.V., 2014. Tectonometamorphic evolution of the Areskutan Nappe - Caledonian history revealed by SIMS U-Pb zircon geochronology, in *New Perspectives on the Caledonides and Related Areas,* pp. 337–368, eds Corfu, F., Gasser, D. & Chew, D., Geological Society, London, Special Publications 390, doi:10.1144/SP390.10.

Lorenz, H., Gee, D.G. & Juhlin, C., 2011. The Scandinavian Caledonides - scientific drilling at mid-crustal level in a Palaeozoic major collisional orogen, *Sci. Drill.,* **11,** 60–63.

Lorenz, H., Almqvist, B.S., Berthet, T. & Klonowska, I., 2015a. The COSC-1 drill core: a geological sample through a hot allochthon and the underlying thrust zone, *Geophys. Res. Abstr.,* **17,** EGU–8337.

Lorenz, H. *et al.*, 2015b. COSC-1 - drilling of a subduction-related allochthon in the Palaeozoic Caledonide orogen of Scandinavia, *Sci. Drill.,* **19,** 1–11.

Lund, C.E., Gorbatschev, R. & Smirnov, A., 2001. A seismic model of the Precambrian crust along the coast of southeastern Sweden: the Coast Profile wide-angle airgun experiment and the southern part of FENNOLORA revisited, *Tectonophysics,* **339**(1–2), 93–111.

Lüschen, E., Bram, K., Söllner, W. & Sobolev, S., 1996. Nature of seismic reflections and velocities from VSP-experiments and borehole measurements at the KTB deep drilling site in southeast Germany, *Tectonophysics,* **264**(1–4), 309–326.

Majka, J., Janak, M., Andersson, B., Klonowska, I., Gee, D.G., Rosen, A. & Kosminska, K., 2014. Pressure-temperature estimates on the Tjeliken eclogite: new insights into the (ultra)-high-pressure evolution of the Seve Nappe Complex in the Scandinavian Caledonides, in *New Perspectives on the Caledonides and Related Areas,* pp. 369–384, eds Corfu, F., Gasser, D. & Chew, D., Geological Society, London, Special Publications 390, doi:10.1144/SP390.14.

Moser, T.J., 1991. Shortest path calculation of seismic rays, *Geophysics,* **56**(1), 59–67.

Palm, H., 1984. Time-delay interpretation of seismic refraction data in the Caledonian front, Jamtland, central Scandinavian Caledonides, *Geol. Föreningen i Stock. Förhandlingar,* **106**(1), 1–14.

Palm, H. & Lund, C.E., 1980. A seismic refraction study in the Caledonian front of Jamtland, Sweden, *Geol. Föreningen i Stock. Förhandlingar,* **102**(4), 561–568.

Palm, H., Gee, D.G., Dyrelius, D. & Björklund, L., 1991. A Reflection seismic image of Caledonian structure in central Sweden, *Sveriges Geol. undersökning,* **75,** 1–36.

Park, C.B., Miller, R.D., Steeples, D.W. & Black, R.A., 1996. Swept impact seismic technique (SIST), *Geophysics,* **61**(6), 1789–1803.

Rawlinson, N. & Sambridge, M., 2003. Seismic traveltime tomography of the crust and lithosphere, *Adv. Geophys.,* **46,** 81–198.

Riedel, M., 2016. Efficient computation of seismic traveltimes in anisotropic media and the application in pre-stack depth migration, *PhD thesis,* TU Bergakademie Freiberg.

Roberts, D., 2003. The Scandinavian Caledonides: event chronology, palaeogeographic settings and likely modern analogues, *Tectonophysics,* **365**(1–4), 283–299.

Schmidt, J., 2000. Deep seismic studies in the western part of the Baltic Shield, *PhD thesis,* Uppsala University.

Streule, M.J., Strachan, R.A., Searle, M.P. & Law, R.D., 2010. Comparing Tibet-Himalayan and Caledonian crustal architecture, evolution and mountain building processes, in *Continental Tectonics and Mountain Building: The Legacy of Peach and Horne,* pp. 207–232, eds Law, R.D., Butler, R.W.H., Holdsworth, R.E., Krabbendam, M. & Starchan, R.A., Geological Society, London, Special Publications 335.

Strömberg, A., Karis, L., Zachrisson, E., Sjöstrand, T., Skoglund, R., Lundegårdh, P. & Gorbatschev, R., 1984. Berggrundskarta över Jämtlands län utom förutvarande Fjällsjö kommun, scale 1:200 000, *Sveriges Geol. undersökning,* Ca 53*,* Uppsala, Sweden.

Thomsen, L., 1986. Weak elastic anisotropy, *Geophysics,* **51**(10), 1954–1966.

Tsvankin, I., 2001. *Seismic Signatures and Analysis of Reflection Data in Anisotropic Media,* Pergamon.

Vidale, J., 1988. Finite-difference calculation of travel-times, *Bull. seism. Soc. Am.,* **78**(6), 2062–2076.

Wenning, Q.C., 2015. Physical rock property and borehole stress measurements from the COSC-1 borehole, Are, Sweden, *MSc thesis,* ETH Zürich.

Wenning, Q.C., Almqvist, B.S.G., Hedin, P. & Zappone, A., 2016. Seismic anisotropy in mid to lower orogenic crust: Insights from laboratory measurements of Vp and Vs in drill core from central Scandinavian Caledonides, *Tectonophysics,* **692,** 14–28.

Yan, P., Garcia Juanatey, M.A., Kalscheuer, T., Juhlin, C., Hedin, P., Savvaidis, A., Lorenz, H. & Kück, J., 2016. A magnetotelluric investigation of the Scandinavian Caledonides in western Jämtland, central Sweden, using the COSC-1 borehole logs as prior information, *Geophys. J. Int.,* **208,** 1465–1489.

Zhang, J. & Toksöz, M., 1998. Nonlinear refraction traveltime tomography, *Geophysics,* **63**(5), 1726–1737.